Nuclear Spin Incoherent Neutron Scattering from Quantum Well Resonators

Max Wolff,[1,*] Anton Devishvili,[1,4] Joseph A. Dura,[2] Franz A. Adlmann,[1] Brian Kitchen,[1] Gunnar K. Pálsson,[1] Heikki Palonen,[1] Brian B. Maranville,[2] Charles F. Majkrzak,[2] and Boris P. Toperverg[3,4]

[1]*Department for Physics and Astronomy, Uppsala University, Regementsvägen 1, 75237 Uppsala, Sweden*

[2]*NIST Center for Neutron Research, National Institute for Standards and Technology, 100 Bureau Drive, Gaithersburg, Maryland 20899, USA*

[3]*Petersburg Nuclear Physics Institute, Leningrad Oblast, 188300 Gatchina, Russia*

[4]*Institut Laue Langevin, 71 Avenue des Martyrs, 38000 Grenoble, France*

(Received 26 December 2018; revised manuscript received 12 April 2019; published 1 July 2019)

We report the detection and quantification of nuclear spin incoherent scattering from hydrogen occupying interstitial sites in a thin film of vanadium. The neutron wave field is enhanced in a quantum resonator with magnetically switchable boundaries. Our results provide a pathway for the study of dynamics at surfaces and in ultrathin films using inelastic and/or quasielastic neutron scattering methods.

DOI: 10.1103/PhysRevLett.123.016101

Surface science has advanced enormously in recent decades, but many scientific questions are not resolved. For example, spin wave dispersions studied using inelastic scanning tunneling microscopy [1,2] and spin-polarized electron loss spectroscopy [3] are in contrast to the theory, and a difference in the potential defining the zero point energy of H adsorbed at Pt and Si surfaces was extracted from nuclear reaction analysis [4]. The surface dynamics of glass formers is under discussion as well [5], and it was shown that the glass transition temperature decreases with a decreasing film thickness [6] together with an enhanced surface mobility [7,8], but it is largely unaffected [9] or slowed down [10] close to a substrate. In self-assembled monolayers, the dynamics depends on the phase, chain length, and functional groups [11]. An important aspect in biology is the dynamics of water close to membranes, which is significantly different from the bulk [12], with a subdiffusive translational motion and an orientational relaxation not described by a single exponential. The dynamics of water in membranes strongly depends on the head groups [13]. Finally, understanding the dynamics of lithium [14] and protons [15] in thin films is crucial for the development of batteries, fuel cells, sensors, and biology [16].

The studies above rely on molecular dynamics simulations or spectroscopy using charged particles with a limited probing depth (or direct contact with a sample, e.g., atomic force microscopy) possibly biasing the results. Other methods probe macroscopic quantities, like, e.g., viscosity. The use of photons in the visible range is restricted to small momentum transfers and subject to various selection rules.

Neutrons interact via the strong force with nuclei and have a spin and thermal energies which probe the whole Brillouin zone, allowing studies of phonon [17] or magnon dispersions. The spin of the neutron in combination with a nuclear moment may result in nuclear spin incoherent scattering (NSIS), making them directly sensitive to tracer diffusion [18,19] and vibrational modes [20]. In surface science, the density profile across an interface is extracted from specular neutron reflectivity (NR). Only a few studies probe in-plane structures [21]. One study from the 1980s reports the dynamics of surface acoustic waves [22] and, recently, the dynamics of a bicontinuous polymer close to a substrate [23].

One way to overcome the intrinsically limited brilliance of neutron sources is the use of quantum resonators [24] from which the scattering can be modeled in the framework of the distorted-wave Born approximation [25]. Utilizing this principle, the absorption and subsequent emission of gamma radiation [26] or alpha particles [27] as well as diffraction [28] and off-specular scattering from magnetic domains [29] were detected.

In this Letter, we use wave field enhancement in quantum resonators combined with magnetic contrast variation [30]. We control the neutron wave amplitude and unambiguously detect NSIS from protons at interstitial lattice sites in a thin film of V, paving the road for future studies of dynamics.

Fe/V superlattices can be grown by rf magnetron sputtering with exceptional crystal quality on MgO substrates [31] (2×2 cm^2 in our case). However, pure V layers are expected to show some defects resulting from strain relaxation at distances farther from the substrate. The ~100-nm-thick V layer, pure (SV) or loaded with H to $H/V = 1/2$ ($SVH_{0.5}$), is sandwiched between two Fe and V layers of 16 and 0.75 nm, respectively. On top, Al_2O_3 and Pd (only Pd for SV) are deposited to prevent both oxidation and H from leaving the sample and to catalyze the dissociation of H_2, respectively. To grow the Al_2O_3, the top V layer had to be exposed to air and is expected to be oxidized.

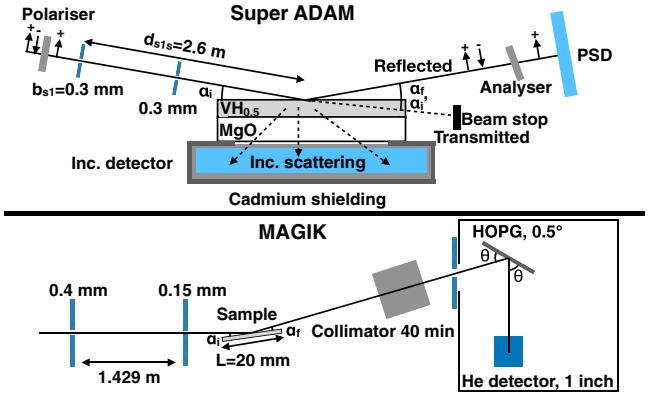

FIG. 1. Schematics of the experimental setup at Super ADAM (top) and MAGIK (bottom) with the sample right in front of a neutron detector or an HOPG analyzer crystal installed, respectively. Dimensions are not to scale.

Measurements were performed at Super ADAM (ILL, Grenoble, France) [32] using $\lambda = 5.183$ Å ($(\Delta\lambda/\lambda) = 0.5\%$). First, the NR of SV was measured in a saturation field of 0.8 T (for Fe), with polarization analysis. Then, a second neutron detector was installed directly behind the samples and wrapped with cadmium, only leaving a small, 2×2 cm^2, window pointing towards the samples to simultaneously detect the NSIS. For these measurements the sample was in a remanent magnetic state, since the second neutron detector did not fit between the coils of the electromagnet. Energy analysis of the NSIS neutrons was implemented on MAGIK [33] [NIST Center for Neutron Research (NCNR), NIST, Gaithersburg, MD, USA] using $\lambda = 0.5$ nm ($(\Delta\lambda/\lambda) \approx 1\%$). The instrument was operated in a three-axis configuration with a HOPG analyzer crystal, without polarization and with the sample magnetized by permanent magnets. A collimator (acceptance 0.65°) was used in front of the analyzer. Both experimental setups are shown in Fig. 1. The NR on Super ADAM (Fig. 2) was taken with a relaxed collimation, 1 mm width of both collimating slits.

Figure 2 (main panel) depicts the measured NR of SV together with a fit obtained with the supermatrix iterative formalism [34]. Error bars throughout this Letter represent one standard deviation. The spin-flip (SF) signal results from tiny imperfections of the polarization setup taken into

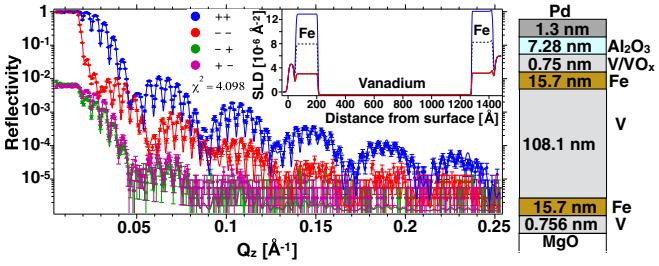

FIG. 2. NR and SLD profile (top right) of SV in saturation. A schematic of the sample is shown on the right-hand side.

TABLE I. Cross sections [10^{-24} cm^2] for the elements relevant for our study [35].

Element	V	H	Fe	Mg	O	Al
$\sigma_{\text{tot,coh}}$	0.0184	1.7568	11.22	3.631	4.232	1.495
$\sigma_{\text{tot,coh,mag}}$	...	...	4.4 [36]	...	...	...
$\sigma_{\text{tot,incoh}}$	5.08	80.26	0.4	0.08	0.0008	0.0082
$\sigma_{\text{tot,abs}}$	5.08	0.3326	2.56	0.063	0.000 19	0.231

account when fitting the data. On the right side, the structure of SV and layer thicknesses extracted from x-ray reflectivity are shown. Almost no damping of the Kiessig fringes is visible, proving exceptionally flat interfaces. The inset depicts the scattering length density (SLD) profiles extracted from the best fit to the NR of SV. The neutron SLD of V is slightly negative, whereas that of Fe is relatively large and positive forming a potential well. Moreover, Fe is magnetic, resulting in different SLDs (indicated by red and blue) depending on the orientation of the neutron spin relative to the direction of the magnetic induction. By using polarized neutrons, the height of the potential well can be tuned and the wave field in the V layer can be controlled. Table I summarizes the total bound coherent, $\sigma_{\text{tot,coh}}$, incoherent scattering, $\sigma_{\text{tot,incoh}}$, and absorption, $\sigma_{\text{tot,abs}}$, cross sections of the elements in the sample.

Figure 3 depicts the calculated wave field $\langle\Psi|\Psi\rangle$ [34] for SV plotted as a color map over the distance from the sample surface and incident beam angle, α_i, for $\lambda = 5.318$ Å and the SLD profiles depicted in Fig. 2 for the $++$ and $--$ polarizations. At angles α_i, where the reciprocal momentum matches the resonance conditions, a standing wave forms with an increased amplitude of the neutron wave function resulting in an increased probability for NSIS. Under these conditions tunneling into the MgO substrate is increased as shown in Fig. 3. Note that $\sigma_{\text{tot,incoh,H}} > 10^3 \sigma_{\text{tot,incoh,Mg}}$ (Table I). For $+$ polarized neutrons, the Fe

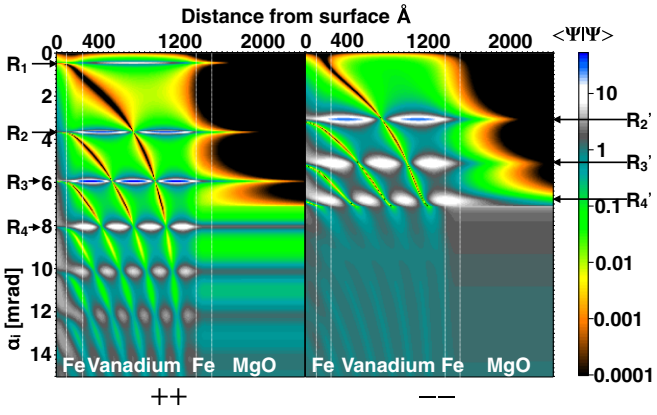

FIG. 3. Amplitude of the wave field, calculated as a function of the depth in SV and α_i. The resonances are marked to aid in later discussions.

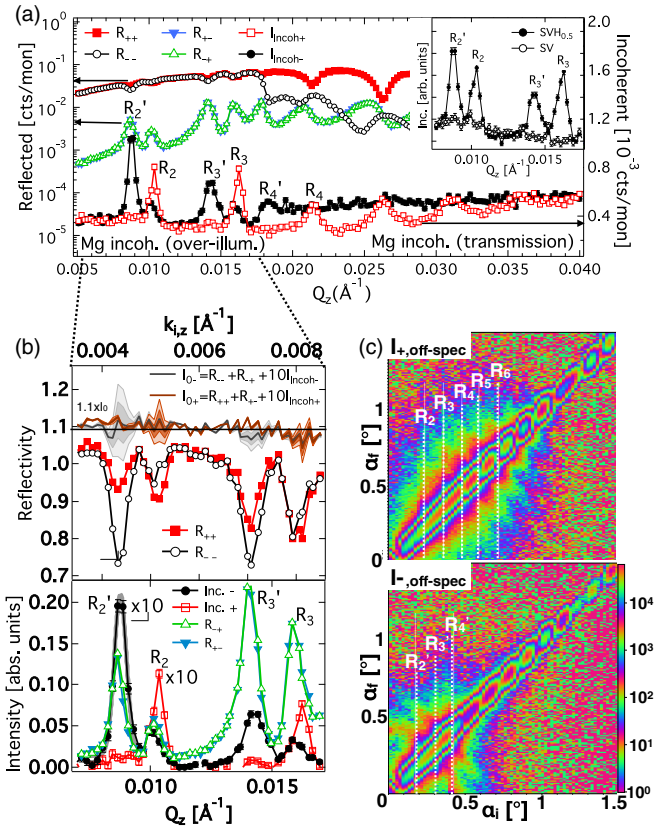

FIG. 4. (a) Reflected intensity [counts normalized by monitor] (left axis) and NSIS (right axis) of $SVH_{0.5}$. The inset upper right depicts a comparison of the NSIS from SV and $SVH_{0.5}$. (b) Low Q region of the NR (upper panel), SF, and NSIS (lower panel) plotted on a linear scale in absolute units (lines are guides to the eye). (c) Off-specular scattering plotted as a color map for different α_i and exiting beam angles α_f.

has a large SLD and the quantum resonator contains only the V (Fig. 3, left panel). For the $-$ polarized beam, the Fe SLDs is below the surrounding MgO and Al_2O_3 SLD (Fig. 2 inset) and, thereby, the resonances are shifted.

Figure 4(a) depicts the NR (red squares and open black circles), SF scattering (blue and green triangles), and the signal from the detector directly behind the sample (open red squares and black circles) of $SVH_{0.5}$ for small Q. The asymmetry in the off-specular scattering combined with the resolution when extracting the specular signal results in the small asymmetry for some of the peaks at the resonance positions. The Fe/V $\langle 010\rangle$ and $\langle 001\rangle$ directions were along the neutron spin quantization axis and surface normal, respectively. In remanence, the magnetization is expected to orient along an easy axis ($\langle 110\rangle$ in thin films of bcc Fe). This gives rise to substantially enhanced SF scattering at the resonances (Fig. 4). A least-squares fit of the data reveals an average tilt angle of the magnetic induction of 34°, resulting from 86.6% and 13.4% of the domains oriented along an easy and hard axis, respectively. This results in a reduction of 17% of the resonator height compared to the saturated sample. In addition, smaller domains, responsible for the weak off-specular scattering, reduce the mean value of the magnetic SLD by about 5%.

At the resonance condition, the wave field is enhanced in the $VH_{0.5}$ layer (similar to that shown in Fig. 3 for SV) and NSIS is detected. Depending on the polarization, the NSIS is dominantly detected at different Q_z values; e.g., NSIS from $(++)$ and $(--)$ is mostly detected for the resonances R_2 and R_2', respectively. The same holds for R_3, R_3' and R_4, R_4'. The inset (upper right) shows the incoherent scattering from SV and $SVH_{0.5}$ scaled to each other. No NSIS is detected for SV. In addition to the sharp peaks, a flat background emerges from the Mg in the substate. This results from overillumination and hitting of the front edge of the sample for $Q_z < 0.018$ Å^{-1}. For $Q_z > 0.018$ Å^{-1}, exceeding the critical value, neutrons are transmitted through the $VH_{0.5}$ and scattered inside the MgO. For experiments run in transmission geometry, the thickness ratio of the film and substrate has to be larger than $(\sigma_{\mathrm{tot,incoh,substrate}}/\sigma_{\mathrm{tot,incoh,film}})$ to get a dominating NSIS from the film.

The total flux of neutrons must be conserved: The sum of transmission T, absorption A, non-SF I_{NSF}, SF I_{SF}, and NSIS I_{inc} must be equal to the incident beam

$$I_0 = T + I_{\mathrm{NSF}} + I_{\mathrm{SF}} + I_{\mathrm{inc}} + A. \tag{1}$$

To calculate the total NSIS, which is isotropic, we scale the neutrons collected $I_{\mathrm{inc}}^{\mathrm{det}}$ by the solid angle in all directions, 4π, divided by the detector solid angle $(d\sigma/d\Omega)_{\mathrm{inc\ det}} = (\pi/2)$, assuming scattering angles of $90° \pm 45°$ around the $-z$ direction (Fig. 1):

$$I_{\mathrm{inc}} = 4\pi \left(\frac{d\sigma}{d\Omega}\right)^{-1}_{\mathrm{inc\ det}} I_{\mathrm{inc}}^{\mathrm{det}} = 8 I_{\mathrm{inc}}^{\mathrm{det}}. \tag{2}$$

Furthermore, we assume zero transmission, which holds for resonances below the critical edge (Fig. 3), and get

$$I_0 = I_{\mathrm{NSF}} + I_{\mathrm{SF}} + A + 8 I_{\mathrm{inc}}^{\mathrm{det}}. \tag{3}$$

The SF reflectivities $(+-)$ and $(-+)$ are equal as expected in the absence of symmetry breaking. The non-SF channels $(++)$ and $(--)$, however, have different reflectivities at the resonances, since the resonator is different for the two incident spin states. Considering Eq. (3), this difference is attributed to absorption, off-specular or NSIS. The NSIS to absorption ratio for $VH_{0.5}$ is $(\sigma_{\mathrm{tot,incoh}}/\sigma_{\mathrm{tot,abs}}) = \frac{9}{1}$ (Table I). Figure 4(c) depicts off-specular scattering from $SVH_{0.5}$ for $+$ and $-$ polarized neutrons. At the positions of the quantum resonances, the off-specular scattering is on a level of 1% of the NR. Taking this into account, we assume an effective reduced (by 25%) incoherent detector cross section and merge the effects by additional scaling of I_{inc}.

We obtain a relation between the difference in R_{++} and R_{--} and the respective difference in the incoherent signal:

$$10(I^{\mathrm{det}}_{\mathrm{inc}--} - I^{\mathrm{det}}_{\mathrm{inc}++}) = R_{++} - R_{--}. \quad (4)$$

Figure 4(b) depicts the very low Q_z region of the NR measured for $SVH_{0.5}$ corrected for the footprint and scaled by I_0 (upper part). In the lower part, $I^{\mathrm{det}}_{\mathrm{inc}}$, with the background from the Mg subtracted and multiplied by 10 and R_{SF}, are plotted on an absolute scale. The gray and brown lines represent I_0 (shifted up by 0.1 for clarity) calculated according to Eq. (3) with the scaling factor of 10 as assumed for Eq. (4). To estimate the sensitivity with respect to the scaling of $I^{\mathrm{det}}_{\mathrm{inc}}$, the light and darker gray and brown areas surrounding the I_0 sum curves indicate a variation of ± 5 and ± 2.5 up and down, respectively. We find that in total 16% of the neutrons are scattered incoherently at R'_2. This is comparable to the 10% typically used for quasielastic studies. Note that, in the present case, neutrons leave the sample as soon as they are scattered incoherently, due to the aspect ratio of the thin film, avoiding multiple scattering. The thickness of a sample of $VH_{0.5}$ in transmission geometry, i.e., without the resonance effect, that also scatters 16% of the incident beam incoherently can be calculated from the number density of scatterers and is 4.8×10^{-4} m. The projected path length in the thin film at R'_2 is 2.66×10^{-5} m. This results in a resonant coherent amplification of 18 consistent with $\int_{\mathrm{VH}_{0.5}} \langle \Psi | \Psi \rangle dz = 23$ calculated from the simulation of the wave field (Fig. 3).

In order to determine if the NSIS is inelastic, we have done another experiment at MAGIK (Fig. 1). Figure 5(a) depicts the intensity detected with an one-inch-diameter He detector by scanning α_i with $\alpha_i + \alpha_f = 3°$. The analyzer angle was set to $\theta = 48.1°$ (elastic condition). Data are shown for $SVH_{0.5}$ (black closed symbols) and SV (red open symbols). The signal at the resonances is enhanced for $SVH_{0.5}$. The highest intensity is found for $\alpha_i = 0.355°$ (at R_3) and $SVH_{0.5}$. For SV, the point with a larger count rate results from $\sigma_{\mathrm{tot,incoh}}$ of V (1/16 that of H). For $\alpha_i = 0.355°$ (at R_3), the scattering or detector angle α_f was scanned [Fig. 5(b)]. The signal is dominated by small angle scattering, resulting from either multiple scattering or macroscopic density fluctuations in the $VH_{0.5}$ studied at room temperature below the critical temperature for phase separation of the α and β phase [37]. Note that the detector at Super ADAM was mounted at a scattering angle of 90°. Figure 5(c) shows data from a $\theta - 2\theta$ scan (inelastic scan) of the analyzer or detector for $\alpha_f = 2.145°$ (avoiding small angle scattering but still leaving enough intensity) and at $\alpha_i = 0.355°$ (R_3). The fitted Gaussian (dashed) line width is resolution limited; therefore, no appreciable inelastic scattering could be observed under these conditions. The contribution of translational diffusion of H in V to the line width grows as Q^2, so the energy transfer is too small to be resolved in a triple-axis setup at the small Q probed.

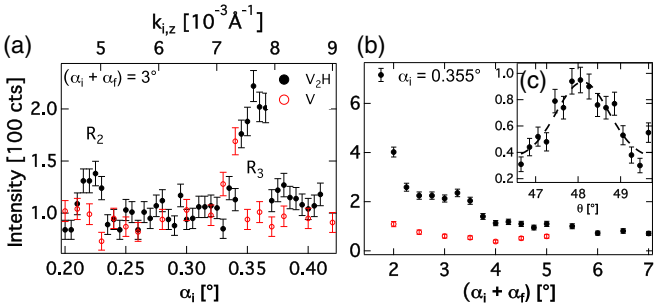

FIG. 5. (a) Elastic NSIS as registered with the HOPG analyzer in place for $\alpha_i + \alpha_f = 3°$. (b) Detector scan with the incident momentum fixed to resonance R_3 at $\alpha_i = 0.355°$. (c) Inelastic scan of the analyzer angle θ.

The FWHM [Gaussian fit, gray line Fig. 4(b)] of R'_2 is $3.56(17) \times 10^{-4}$ Å^{-1} or $(\Delta Q/Q) \approx 4\% \approx (\Delta\alpha_i/\alpha_i)$. This narrow acceptance imposes challenges for instruments using a polychromatic beam for which the incident wavelength has to be dispersed [38–40] and refocused [41] to meet the resonance condition. Direct geometry chopper time of flight spectrometers offer a flexible incident wavelength resolution, a large detector area (on the order of $(\pi/2)$), and a monochromatic beam. With the choppers open, the incoherent signal can be captured. We detected 25 neutrons/s at resonance R'_2 on Super ADAM. An optimization of $(\Delta\lambda/\lambda)$ to meet $(\Delta\alpha_i/\alpha_i)$ can provide a gain factor of up to eight (200 neutrons/s). Note that, ultimately, the brilliance is defined by the source or moderator. Once aligned, the beam might be chopped (not required at a spallation source) to allow energy analysis. We propose to measure only the energy gain side to maximize the pulse repetition rate. On a dedicated beam line optimized in all respects, further gain factors can be expected.

In summary, we have detected nuclear spin incoherent scattered neutrons from a film as thin as 100 nm. The controllable enhanced signal at the resonances in a potential well allows an unambiguous discrimination between a signal from the layer of interest and background. Experiments following along the lines presented here provide a pathway for studies of dynamics in thin films and at interfaces with neutron spectroscopy.

Financial support by the Swedish research council (Grant No. 2012-05115) is acknowledged.

*max.wolff@physics.uu.se

[1] T. Balashov, A. F. Takács, W. Wulfhekel, and J. Kirschner, Magnon Excitation with Spin-Polarized Scanning Tunneling Microscopy, Phys. Rev. Lett. **97**, 187201 (2006).

[2] C. L. Gao, A. Ernst, G. Fischer, W. Hergert, P. Bruno, W. Wulfhekel, and J. Kirschner, Spin Wave Dispersion on the Nanometer Scale, Phys. Rev. Lett. **101**, 167201 (2008).

[3] J. Prokop, W. X. Tang, Y. Zhang, I. Tudosa, T. R. F. Peixoto, K. Zakari, and J. Kirschner, Magnons in a Ferromagnetic Monolayer, Phys. Rev. Lett. **102**, 177206 (2009).
[4] K. Fukutani, A. Itoh, M. Wilde, and M. Matsumoto, Zero-Point Vibration of Hydrogen Adsorbed on Si and Pt Surfaces, Phys. Rev. Lett. **88**, 116101 (2002).
[5] M. D. Ediger and J. A. Forrest, Dynamics near free surfaces and the glass transition in thin polymer films: A view to the future, Macromolecules **47**, 471 (2014).
[6] Z. Yang, Y. Fujii, F. K. Lee, C.-H. Lam, and O. K. C. Tsui, Glass transition dynamics and surface layer mobility in unentangled polystyrene films, Science **328**, 1676 (2010).
[7] Z. Fakhraai and J. A. Forrest, Measuring the surface dynamics of glassy polymers, Science **319**, 600 (2008).
[8] L. Zhu, C. W. Brian, S. F. Swallen, P. T. Straus, M. D. Ediger, and L. Yu, Surface Self-Diffusion of an Organic Glass, Phys. Rev. Lett. **106**, 256103 (2011).
[9] M. Tress, E. U. Mapesa, W. Kossack, W. K. Kipnusu, M. Reiche, and F. Kremer, Surface self-diffusion of an organic glass, Science **341**, 1371 (2013).
[10] R. D. Priestley, C. J. Ellison, L. J. Broadbelt, and J. M. Torkelson, Structural relaxation of polymer glasses at surfaces, interfaces, and in between, Science **309**, 456 (2005).
[11] A. Badia, R. B. Lennox, and L. Reven, A dynamic view of self-assembled monolayers, Acc. Chem. Res. **33**, 475 (2000).
[12] B. Bagchi, Water dynamics in the hydration layer around proteins and micelles, Chem. Rev. **105**, 3197 (2005).
[13] K. Murzyn, W. Zhao, M. Karttunen, M. Kurdziel, and T. Rog, Dynamics of water at membrane surfaces: Effect of headgroup structure, Biointerphases **1**, 98 (2006).
[14] S. Kalinin, N. Balke, S. Jesse, A. Tselev, A. Kumar, T. M. Arruda, S. Guo, and R. Porksch, Li-ion dynamics and reactivity on the nanoscale, Mater. Today **14**, 548 (2011).
[15] M. R. Karim, K. Hatakeyama, T. Matsui, H. Takehira, T. Taniguchi, M. Koinuma, Y. Matsumoto, T. Akutagawa, T. Nakamura, S.-I. Noro, T. Yamada, H. Kitagawa, and S. Hayami, Graphene oxide nanosheet with high proton conductivity, J. Am. Chem. Soc. **135**, 8097 (2013).
[16] A. Royant, K. Edman, T. Ursby, E. Pebay-Peyroula, E. M. Landau, and R. Neutze, Helix deformation is coupled to vectorial proton transport in the photocycle of bacteriorhodopsin, Nature (London) **406**, 645 (2000).
[17] B. N. Brockhouse, Lattice Vibrations in Silicon and Germanium, Phys. Rev. Lett. **2**, 256 (1959).
[18] M. Beè, *Quasielastic Neutron Scattering* (Adam Hilger, Bristol, 1988).
[19] R. Hempelmann, *Quasielastic Neutron Scattering and Solid State Diffusion* (Clarendon Press, Oxford, 2000).
[20] P. C. H. Mitchell, S. F. Parker, A. J. Ramirez-Custa, and J. Tomkinson, *Vibrational Spectroscopy with Neutrons* (World Scientific, Singapore, 2005).
[21] M. Wolff, Grazing incidence scattering, EPJ Web Conf. **188**, 04002 (2018).
[22] W. A. Hamilton, A. G. Klein, G. I. Opat, and P. A. Timmins, Neutron Diffraction by Surface Acoustic Waves, Phys. Rev. Lett. **58**, 2770 (1987).
[23] S. Jaksch, O. Holderer, M. Gvaramia, M. Ohl, M. Monkenbusch, and H. Frielinghaus, Nanoscale rheology at solid-complex fluid interfaces, Sci. Rep. **7**, 4417 (2017).
[24] F. Pfeiffer, V. Leiner, P. Høghøj, and I. Anderson, Submicrometer Coherent Neutron Beam Production Using a Thin-Film Waveguide, Phys. Rev. Lett. **88**, 055507 (2002).
[25] Z. Jiang, D. R. Lee, S. Narayanan, J. Wang, and S. K. Sinha, Waveguide-enhanced grazing-incidence small-angle x-ray scattering of buried nanostructures in thin films, Phys. Rev. B **84**, 075440 (2011).
[26] H. Zhang, P. D. Gallagher, S. K. Satija, R. M. Lindström, R. L. Paul, T. P. Russell, P. Lambooy, and E. J. Kramer, Grazing Incidence Prompt Gamma Emissions and Resonance-Enhanced Neutron Standing Waves in a Thin Film, Phys. Rev. Lett. **72**, 3044 (1994).
[27] V. L. Aksenov, Y. V. Nikitenko, F. Radu, Y. M. Gledenov, and P. V. Sedyshev, Observation of resonance enhanced neutron standing waves through (n,α) reaction, Physica (Amsterdam) **276B–278B**, 946 (2000).
[28] H. Zhang, S. K. Satija, P. D. Gallagher, J. A. Dura, K. Ritley, C. P. Flynn, and J. F. Ankner, Diffraction of neutron standing waves in thin films with resonance enhancement, Physica (Amsterdam) **221B**, 450 (1996).
[29] F. Radu, V. Leiner, K. Westerholt, H. Zabel, J. McCord, A. Vororbiev, J. Major, D. Jullien, H. Humblot, and F. Tasset, Magnetic induction and domain walls in magnetic thin films at remanence, J. Phys. Condens. Matter **17**, 1711 (2005).
[30] S. A. Holt, A. P. Le Brun, C. F. Majkrzak, D. J. McGillivray, F. Heinrich, M. Lösche, and J. H. Lakey, An ion-channel-containing model membrane: structural determination by magnetic contrast neutron reflectometry, Soft Matter **5**, 2576 (2009).
[31] S. A. Droulias, G. K. Palsson, H. Palonen, A. Hasan, K. Leifer, V. Kapaklis, B. Hjrvarsson, and M. Wolff, Crystal perfection by strain engineering: The case of Fe/V (001), Thin Solid Films **636**, 608 (2017).
[32] A. Devishvili, K. Zhernenkov, A. J. C. Dennison, B. P. Toperverg, M. Wolff, B. Hjrvarsson, and H. Zabel, SuperADAM: Upgraded polarized neutron reflectometer at the Institut Laue-Langevin, Rev. Sci. Instrum. **84**, 025112 (2013).
[33] J. Dura, D. Pierce, C. Majkrzak, N. Maliszewskyj, D. McGillivray, M. Loesche, K. O'Donovan, M. Mihailescu, U. Perez-Salas, D. Worcester, and S. White, AND/R: Advanced neutron diffractometer/reflectometer for investigation of thin films and multilayers for the life sciences, Rev. Sci Instrum. **77**, 074301 (2006).
[34] B. P. Toperverg, Polarized neutron reflectometry of magnetic nanostructures, Phys. Met. Metallogr. **116**, 1337 (2015).
[35] V. F. Sears, Neutron scattering lengths and cross sections, Neutron News **3**, 26 (1992).
[36] J. W. Lynn, in *Characterization of Materials*, edited by E. N. Kaufmann (John Wiley & Sons, New York, 2012), p. 1.
[37] L. Schlapbach and A. Züttel, Hydrogen-storage materials for mobile applications, Nature (London) **414**, 353 (2001).
[38] H. Frielinghaus, M. Gvaramia, G. Mangiapia, S. Jaksch, M. Ganeva, A. Koutsioubas, S. Mattauch, M. Ohl, M. Monkenbusch, and O. Holderera, New tools for grazing

incidence neutron scattering experiments open perspectives to study nano-scale tribology mechanisms, Nucl. Instrum. Methods Phys. Res., Sect. A **871**, 72 (2017).

[39] F. Ott and A. Menelle, REFocus: A new concept for a very high flux neutron reflectometer, Nucl. Instrum. Methods Phys. Res., Sect. A **586**, 23 (2008).

[40] F. Ott and A. de Vismes, RefloGrad/GradTOF: Neutron energy analysis for a very high-flux neutron reflectometer, Physica (Amsterdam) **397B**, 153 (2007).

[41] F. Ott and A. Menelle, TilToF: A high-intensity space–time reflectometer, Physica (Amsterdam) **385B–386B**, 985 (2006).